Pore-scale characterization of residual gas remobilization in CO_2 geological storage

Ramin Moghadasi [a,b,*], Sepideh Goodarzi [c], Yihuai Zhang [d], Branko Bijeljic [c], Martin J. Blunt [c], Auli Niemi [b]

[a] *Department of Earth Sciences, University of Gothenburg, Gothenburg, Sweden*
[b] *Department of Earth Sciences, Uppsala University, Uppsala, Sweden*
[c] *Department of Earth Science and Engineering, Imperial College, London, United Kingdom*
[d] *James Watt School of Engineering, University of Glasgow, Glasgow, United Kingdom*

ARTICLE INFO

ABSTRACT

A decrease in reservoir pressure can lead to remobilization of residually trapped CO_2. In this study, the pore-scale processes related to trapped CO_2 remobilization under pressure depletion were investigated with the use of high-resolution 3D X-ray microtomography. The distribution of CO_2 in the pore space of Bentheimer sandstone was measured after waterflooding at a fluid pressure of 10 MPa, and then at pressures of 8, 6 and 5 MPa. At each stage CO_2 was produced, implying that swelling of the gas phase and exsolution allowed the gas to reconnect and flow. After production, the gas reached a new position of equilibrium where it may be trapped again. At the end of the experiment, we imaged the sample again after 30 hours. Firstly, the results showed that an increase in saturation beyond the residual value was required to remobilize the gas, which is consistent with earlier field-scale results. Additionally, Ostwald ripening and continuing exsolution lead to a significant change in fluid saturation: transport of dissolved gas in the aqueous phase to equilibrate capillary pressure led to reconnection of the gas and its flow upwards under gravity. The implications for CO_2 storage are discussed: an increase in saturation beyond the residual value is required to mobilize the gas, but Ostwald ripening can allow local reconnection of hitherto trapped gas, thus enhancing migration and may reduce the amount of CO_2 that can be capillary trapped in storage operations.

1. Introduction

Carbon Capture and Storage (CCS) is a key technology to reduce atmospheric CO_2 emissions and thereby prevent climate change (IPCC 2005, Alcalde et al., 2018, Michael et al., 2010). In CCS, the captured anthropogenic CO_2 is injected into deep porous and permeable subsurface media (such as saline aquifers) where it will be retained by processes that act over various spatial and temporal scales (Niemi et al., 2017, Ali et al., 2022, Bui et al., 2018). The main mechanisms that trap the injected CO_2 are structural trapping, residual trapping, dissolution, and mineralization (Zhang and Song, 2014, Lebedev et al., 2017, Lebedev et al., 2017, Yu et al., 2019). The focus in the present study is on residual trapping, a process in which a fraction of the injected CO_2 is immobilized in the form of isolated blobs or ganglia in the pore space by capillary forces, usually after CO_2 injection when water displaces a migrating CO_2 plume (Rasmusson et al., 2018, Qi et al., 2009).

While residual trapping of CO_2 is inherently a pore-scale mechanism, it affects the plume extent over long distances, and its stability contributes significantly to the overall CO_2 storage capacity, safety, and security on both short and long timescales (Krevor et al., 2015). Conventionally, the residual CO_2 ganglia are expected to remain trapped and not become mobile until eventually dissolving into the aqueous (brine) phase, in particular under *in situ* post injection reservoir conditions where viscous forces due to fluid flow are not sufficient for remobilization (Goodman et al., 2011). However, there are several mechanisms and processes where CO_2 saturation can increase leading to remobilization of the trapped gas. An obvious situation is when CO_2 is again injected into the reservoir, which could happen, but is unlikely.

Pressure depletion is another process that can lead to trapped gas remobilization (Kortekaas and van Poelgeest, 1991, Moghadasi et al., 2022, Moghadasi, 2022). This process can be triggered, after the injection has stopped, by any sort of leakage (a leaky wellbore, fracture or

permeable fault; Alcalde et al., 2018; Moghadasi, 2022; Shaffer, 2010; Celia et al., 2011) or simply due to the dissipation of the pressure build-up near the wellbore (Jiang et al., 2014, Shi et al., 2013). It can also be caused during active pressure management (also known as Active CO_2 Reservoir Management, ACRM (Buscheck et al., 2011, Birkholzer et al., 2012)) during which resident brine is extracted to lower the reservoir pressure. During pressure depletion the CO_2 saturation will increase due to both gas expansion and exsolution of CO_2 from the aqueous phase.

With a drop in pressure, remobilization of the residual gas has been shown to take place at a value higher than the residual saturation (where the gas became immobilized). This value is known as the critical gas saturation (S_{gc}) (Moghadasi et al., 2022, Berg et al., 2020, Fishlock et al., 1988, Li and Yortsos, 1993, Ligthelm et al., 1997, McDougall and Sorbie, 1999). Furthermore, even after remobilization the gas will have a substantially lower relative permeability compared to that under primary drainage or imbibition (Moghadasi et al., 2022, Ligthelm et al., 1997, Egermann and Vizika, 2000). While this delayed and slower remobilization of residually trapped gas under pressure depletion conditions is well-established in the context of oil and gas recovery, it has been unnoticed and typically not considered in the context of CO_2 geological storage. Recently, however, the pilot-scale CO_2 injection experiments at Heletz, Israel (Niemi et al., 2020, Joodaki et al., 2020) showed the importance of this process in the CCS context as well. During the second set of experiments, known as the Heletz residual trapping experiments II (RTE-II), the observed delayed tracer arrival could only be explained by introducing a critical gas saturation which was higher than the residual value (Moghadasi et al., 2022). In this field test, the injected partitioning gas tracer was recovered from the residual zone, over the course of 24 hours, which caused a reservoir pressure decline of 0.5 MPa. Due to this occurence, part of the tracer, which was partitioned into the residual gas phase, was not recovered until the gas phase became mobile – at a saturation 5% higher than the residual saturation ($S_{gc} - S_{gr} = 0.05$). This is the first-ever observation of critical gas saturation in CCS at field scale. In CCS, critical saturation is a safety enhancing feature as it delays the flow and migration of the remobilized gas, in comparison to the classical model, where remobilization takes place right after the residual saturation is exceeded. The observations from the Heletz experiments prompted the interest to study this phenomenon and the underlying processes at the pore scale, thus being the motivation for the present study.

The common practice in the oil and gas industry is to quantify the critical gas saturation in the laboratory at the core-scale during which the remobilization of the gas is inferred from flow measurements (Berg et al., 2020). However, these experiments, in addition to being error-prone, are unable to unravel the salient pore-scale physics involved. Recent advances in 3D X-ray micro-computed tomography (micro-CT) have, however, made it possible to non-invasively image and visualize the fluid distribution at micron-scale resolution (at the pore scale) under *in situ* conditions (Andrew et al., 2014, Iglauer et al., 2011, Blunt et al., 2013). This has allowed direct and accurate determination of critical gas saturation. A recent example is the work by Berg et al. (Berg et al., 2020) where they used micro-CT to take direct measurements of the critical gas saturation. Although their work provided valuable insights into the pore-scale physics of gas remobilization under pressure depletion, a model hydrocarbon system was studied, rather than CO_2.

In this work, we used pore-scale imaging to characterize the remobilization of residually trapped CO_2 phase during pressure depletion. Micro-CT images of the distribution of CO_2 were obtained on a system where CO_2 was initially residually trapped by brine and the pressure was stepwise decreased from 10 to 5 MPa. At the end, the system was left for 30 hours at 5 MPa and the final scan was taken. Each scan was reconstructed into a 3D volume on which image analysis was performed.

The remainder of this paper is organized as follows. Section 2 presents an overview of the materials and methods, including X-ray microtomography, and details of the image processing technique. Section 3 presents the results and discusses the main findings of the work. The concluding remarks are in turn presented in the final section 4.

2. Experimental materials and equipment

A Zeiss Xradia 510 Versa micro-CT was used to obtain high-resolution 3D images of the rock sample and the fluids it contained. The sample was a Bentheimer sandstone (typical composition of quartz: 91.7%, feldspar: 4.86%, clay: 2.68%, pyrite and iron hydroxides: 0.17% (Wim Dubelaar and Nijland, 2015, Peksa et al., 2015)). The porosity was approximately 20.4% and the permeability was $1.47 \pm 0.03 \times 10^{-12}$ m^2 (Lin et al., 2018). The sample is naturally water-wet with *in situ* contact angles averaging approximately 48° through water in the presence of both oil and gas (Blunt et al., 2019). The sample had a length of 21.02 mm and diameter of 6.03 mm. The sample was first wrapped in aluminum foil and then tightly fitted into a cylindrical Viton sleeve. It was then inserted into a Hassler-type X-ray transparent carbon fiber core-holder. The core-holder was in turn wrapped with a flexible heating jacket, and then securely mounted on a rotating plate inside the micro-CT apparatus. The top and bottom of the core-holder were connected to flow lines that went outside the scanner. Two thermocouples connected to a PID controller were also attached to the core holder with aluminum tape to measure and control the temperature. Four high-precision syringe pumps (ISCO, model 1000D) were used to inject and receive the fluids, and to apply confining pressure. A schematic of the whole apparatus is shown in Fig. 1.

The aqueous phase was a solution of 3.5 wt.% potassium iodide (KI), which provided an effective X-ray contrast between brine (wetting phase) and CO_2 (non-wetting phase).

2.1. Experimental protocol and image acquisition

The experiment was designed to mimic conditions in an aquifer wherein CO_2 is contained at the residual state, and the system then undergoes pressure depletion. We studied a wide pressure range, starting at 10 MPa, representative of a storage reservoir at a depth of around 1 km with a study of the transition of the CO_2 from a supercritical to a gaseous state.

After loading the sample into the core holder, the following steps were taken:

1. A confining pressure of 1MPa was applied around the sample with deionized water.
2. The core holder was then heated up gradually to reach a temperature of 50 °C.
3. The system was flushed with air to fully dry the sample and the connecting lines. A dry scan was taken.
4. The sample and system were vacuumed for 12 hours, thereafter more than 20 pore volumes (1 PV ≈ 0.12 mL) of KI doped brine that had not been equilibrated with CO_2 were injected from the base at a rate of 0.5 mL/min with 1 MPa back pressure and 2 MPa confining pressure, to fully saturate the sample with brine. Full saturation was confirmed by the absence of any gas bubbles in the fully-saturated scan taken in the next step.
5. The confining pressure and pore pressure were increased by 10 MPa in steps of 1 MPa. A fully brine-saturated scan was taken. A difference of 1 MPa was maintained between confining pressure and pore pressure.
6. Primary drainage: 20 PV of CO_2 was injected from the base at a very low flow rate of 0.04 mL/min (6.66×10^{-10} m^3/s). This corresponds to a capillary number $N_c = \mu v / \sigma$ of around 1.8×10^{-8}, which ensures a capillary dominated regime. Here, μ is the CO_2 viscosity (28.34×10^{-6} Pa.s), v is the Darcy velocity of the injected CO_2, and σ is the CO_2-brine interfacial tension (IFT) (approximately 36×10^{-3} N/m; Iglauer et al., 2011) at the experimental conditions.
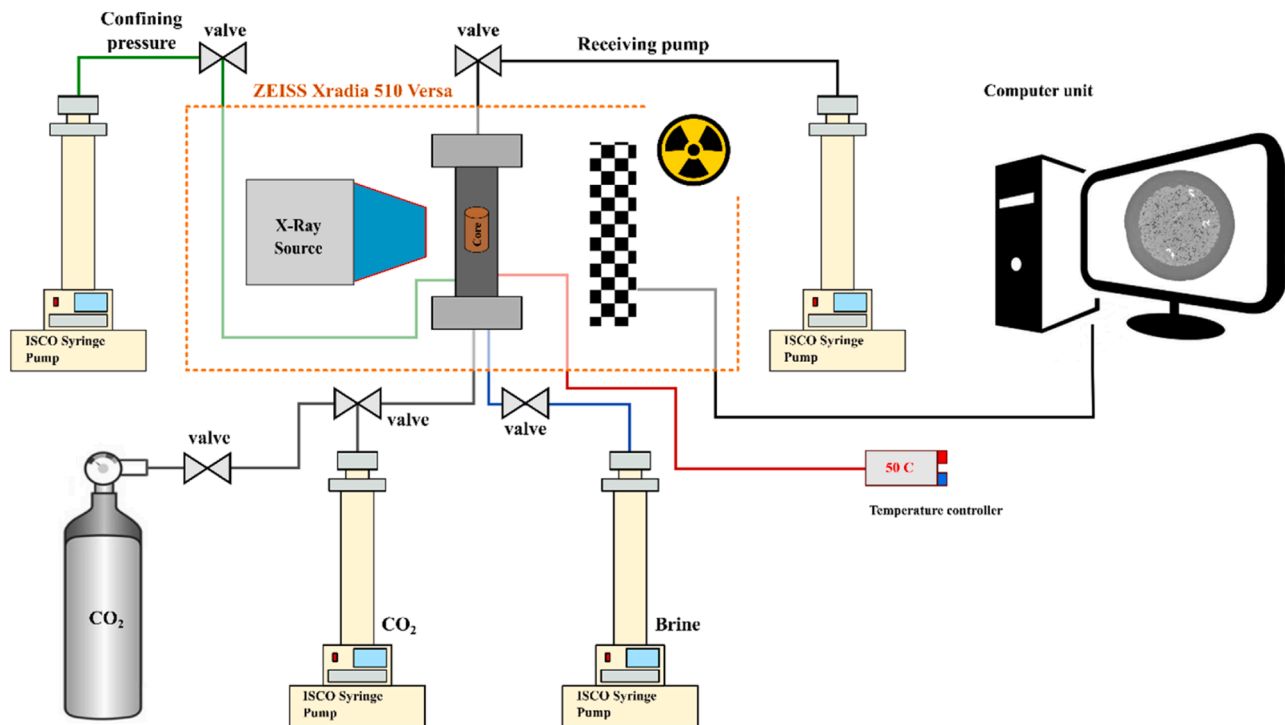
Fig. 1. Schematic presentation of the experimental apparatus.

7. Imbibition: the residual state of CO_2 was established by injecting 2 PV of brine from the base at a very low flow rate of 0.04 mL/min (6.66×10^{-10} m^3/s). Using the brine viscosity of 0.93×10^{-3} Pa.s, the capillary number N_c was determined to be 6×10^{-7}, which ensures a capillary dominated regime.

8. The fluid pressure was reduced in steps of 0.1 MPa to 8, 6 and 5 MPa, while maintaining 1 MPa pressure difference between confining and pore fluid. Each step took approximately 20 minutes to allow pressure equilibrium to be reached. The valves to the receiving and confining pumps were opened to allow this. X-ray CT scanning was performed at each pressure level.

9. The system was finally left at 5 MPa with all valves closed for 30 hours, and the final X-ray CT scan was then taken.

To minimize the fluid rearrangement during the scan, the system was allowed to equilibrate for about 20 min before the scan. This was sufficient time for the average pressure to stabilize, but not necessarily – as we discuss later – for the phase distribution to reach equilibrium. All scans took approximately 75 min to acquire, which consisted of 3001 projections of the sample at regular angular intervals. The projections were in turn reconstructed into a three-dimensional (3D) volume using software on the micro-CT scanner.

2.2. Image processing

In total, 7 images with a voxel size of 3.84 µm were acquired during the experiments including scans of the sample when it was fully dry (i.e., the fluid was air), fully saturated with brine; scans after setting the system's pressure to 10, 8, 6, and 5 MPa, and an additional scan after resting the system for 30 hours at 5 MPa. The images were acquired in the central section of the full sample, over a length of 5.8 mm with 1523 $\times$ 1553 $\times$ 1514 voxels. The images were processed and visualized using Avizo 2020.1 (Thermo-Fisher Scientific) software. For illustrative purposes, a smaller sub-volume of 500 $\times$ 500 $\times$ 1500 voxels was selected to visualize CO_2 ganglia.

The image processing workflow is as follows. First, an edge preserving non-local means filter was applied to remove noise from the

grayscale images and thereby improve the segmentation, which was in turn performed using a seed-watershed algorithm. The algorithm is based on the grayscale intensity of each individual voxel, which allows for the elimination of partial volume artifacts as well as the voxel misidentification that is present with simple grayscale segmentation. The pores and grains were identified from the segmentation of the dry sample, which was then used as the mask for the wet segmented images (when the sample contained brine, CO_2, or both). The porosity obtained from the segmented volume was 20.4 %, which agrees with the reported values on Bentheimer sandstone (Wim Dubelaar and Nijland, 2015, Zhang et al., 2018). The uncertainty in slice-averaged saturation is approximately $\pm5\%$: this is a systematic error, as dependent on the thresholds used in the segmentation all the saturation values can increase or decrease (Raeini et al., 2022). We can, however, accurately compare the differences between images. In this work, the same routine, developed by Raeini et al. (2022), was applied on all images, and thus the uncertainties between different images are minimized. Fig. 2 shows an example slice on which the image processing was applied.

3. Results and discussion

First, in Section 3.1 the results from the analysis of the images at various pressures are presented, including saturation profiles and 3D visualizations that illustrate the connectivity of the gas phase during the depletion sequence. Then, in Section 3.2 pore-scale ganglia rearrangement is investigated when the system was left at 5 MPa for 30 hours (i.e., under no pressure depletion) at the end of the experiment.

3.1. Pore scale ganglion dynamics under pressure depletion

Fig. 3 shows the saturation profile of CO_2 across the length of the image, 5.8 mm, at the end of imbibition when CO_2 is residually trapped. The slice-averaged saturation varies between 0.30 and 0.70, with an average residual saturation S_{gr} of 0.48: this high value is consistent with CO_2 being the non-wetting phase, trapped in the larger pore spaces.

The saturation profiles of CO_2 at the different pressures of 10, 8, 6 and 5 MPa are plotted in Fig. 4. It can be seen that with decreasing
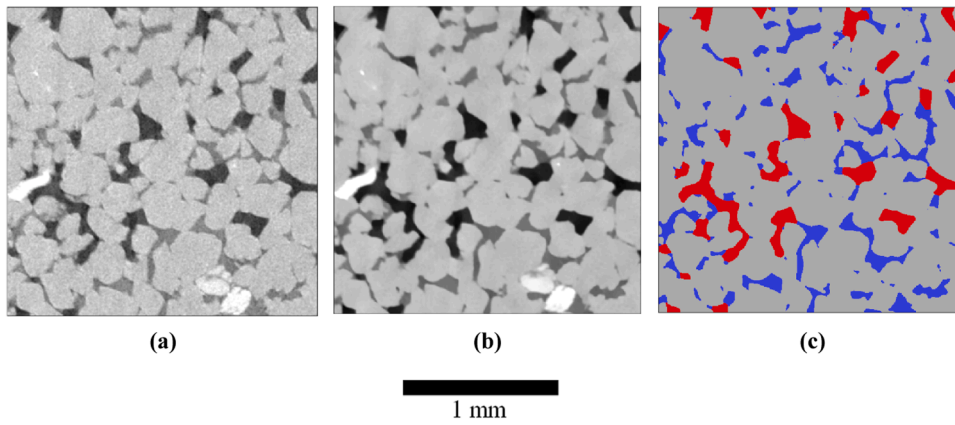
Fig. 2. Image processing workflow illustrated on a two-dimensional cross-section of a three-dimensional image: a) raw image (noisy), b) filtered image (noise removed), c) segmented image (red is CO_2, blue is brine, and gray is rock). Note that the white space in (a) and (b) are minerals that are counted as the rock phase.
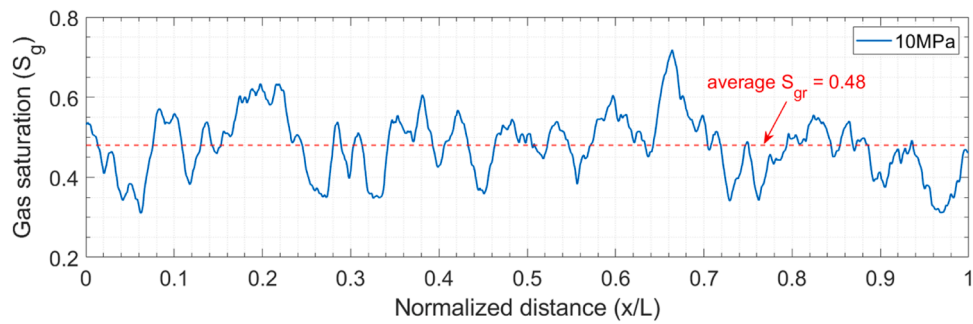
Fig. 3. CO_2 saturation profile at the end of imbibition (water flooding). A central section of the sample, 5.8 mm long, is imaged. The fluids are injected from the left and produced from the right. (x: distance from base of the image, L: length of image, 5.8 mm).
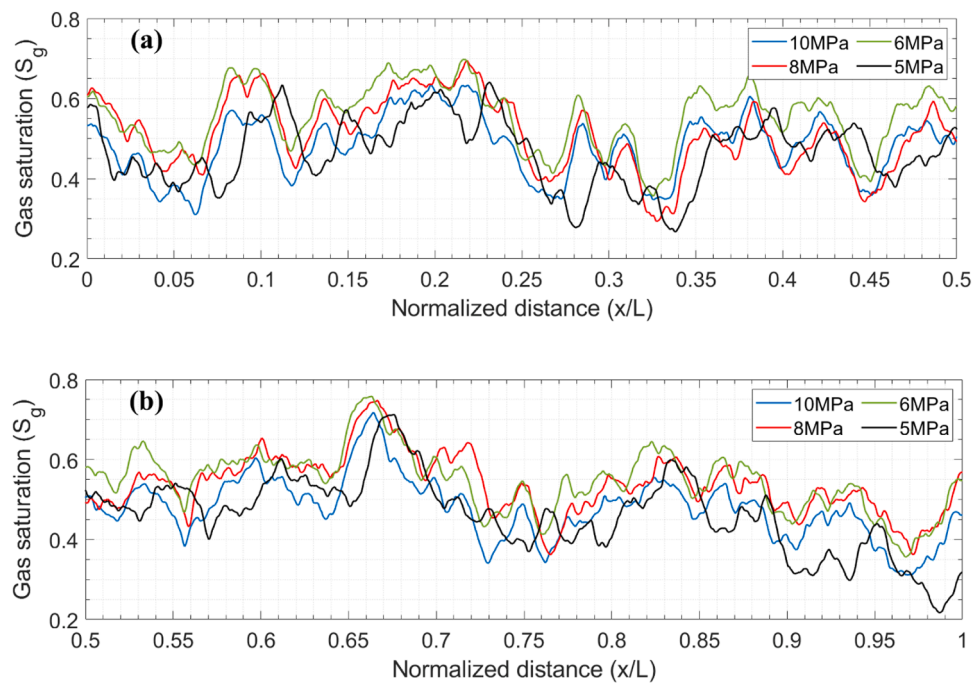
Fig. 4. CO_2 saturation profiles at different pressures from 10 MPa, 8 MPa, 6 MPa, and to 5 MPa: a) from x/L = 0 to x/L = 0.50; b) from x/L = 0.50 to x/L = 1.0 (x: distance from the base of the image, L: length of the image, 5.8 mm).

pressure from 10 to 6 MPa the CO_2 saturation exhibits an increasing trend in the profiles overall, and then decreases once the pressure is reduced to 5 MPa. On average, the CO_2 saturation increases from 0.48 to 0.52 to 0.55, when the pressure is decreased from 10 to 8 to 6 MPa respectively, and then decreases to 0.46 at 5 MPa. The reduction in saturation is particularly noticeable towards the outlet (see Fig. 5b between x/L = 0.85 and x/L = 1.0). Since data on CO_2 density are available (ToolBox, Megawatsoft), we can determine the mass of gas contained in the sample at each pressure. In turn, by material balance, we calculate the amount that leaves the system (i.e., produced) once the pressure is dropped. The calculated values are given in Table 1.

To investigate the gas-phase connectivity, Fig. 5 presents 3D visualizations of the CO_2 at different pressures. At 10 and 8 MPa, there is no a ganglion that is connected across the image. At 6 MPa, however, a near percolating gas ganglion can be seen (shown in red).

We can use the images to interpret what happens during the experiment. As the pressure drops, the gas phase expands. In addition, some gas comes out of solution, and it is assumed that this gas is added to the existing ganglia. Once the gas phase becomes connected across the sample, it can be produced: from Table 1 it is evident that this occurs after each pressure depletion step. Gas production leads to a reduction in saturation: the gas reaches a new position of equilibrium and may become disconnected again through snap-off in some of the narrower pore spaces (Iglauer et al., 2011, Singh et al., 2017). Hence, there is an intermittent process of increases in gas saturation with a drop in pressure, and decreases due to production and aqueous phase reinvasion.

We assume that the residual gas saturation is 0.48 determined from the end of waterflooding at the highest pressure. We assume that at 8 and 5 MPa the saturation is below the critical gas saturation, S_{gc} when a percolating gas ganglion is formed in the sample (Li and Yortsos, 1993, Li and Yortsos, 1995) since we do not observe a connected cluster of gas in the small region we investigated. However, at 6 MPa there is a connected ganglion as evident in Fig. 5 and we make the assumption that the saturation in this image is S_{gc}. The difference between S_{gc} and S_{gr} is referred to as remobilization saturation S_{gmob}. Here, values of S_{gc} and S_{gmob} are determined to be 0.55 and 0.07, respectively from comparing the saturations at 10 MPa after imbibition and at 6 MPa in Table 1.

Reducing the pressure further to 5 MPa, the percolating gas ganglia again loses its connectivity. This further confirms that gas remobilization is intermittent in nature, meaning that a continuous and stable flow of remobilized gas-phase may not be retained during pressure depletion (it is possible that reconnected gas ganglia become disconnected again

due to capillary forces). This could explain the reduced relative permeability of remobilized gas that has been observed in our earlier studies (Moghadasi et al., 2022).

To quantitatively characterize the gas connectivity at different pressures, we quantify the Euler characteristics of the gas phase on the imaged section of the sample. The Euler characteristic is a topological measure of connectivity, and it is calculated as the number of ganglia minus the number of redundant loops inside the ganglia (Herring et al., 2019). A large positive Euler number for a phase indicates that the phase is trapped in discrete, isolated regions or ganglia within the pore space, while a large negative number means that the phase is interconnected with many loops (Alhosani et al., 2021, Alhosani et al., 2021). To calculate the Euler characteristic, we considered a segmented image comprising $1523 \times 1553 \times 1514$ voxels. The initial step involved isolating the gas phase within the image. Subsequently, we utilized the Euler number module within the image analysis software to process the isolated gas phase. The module generates dimensionless Euler characteristic values, which we normalized by dividing them by the total

Table 1

Calculated values of the mass of gas in the sample. Only the mass of CO_2 in its own phase is considered.

Pressure (MPa)	Saturation	Volume ($m^3 \times 10^{-8}$)	Density (kg/m^3)	Mass in place ($kg \times 10^{-6}$)	Produced mass ($kg \times 10^{-6}$)
10	0.48	1.62	384.4	6.23	
8	0.52	1.75	219.2	3.85	2.38 (from 10-8 MPa)
6	0.55	2.51	135.2	2.51	1.33 (from 8-6 MPa)
5	0.46	1.62	104.8	1.62	0.89 (from 6-5 MPa)

Table 2

Euler characteristics per unit volume of the gas phase.

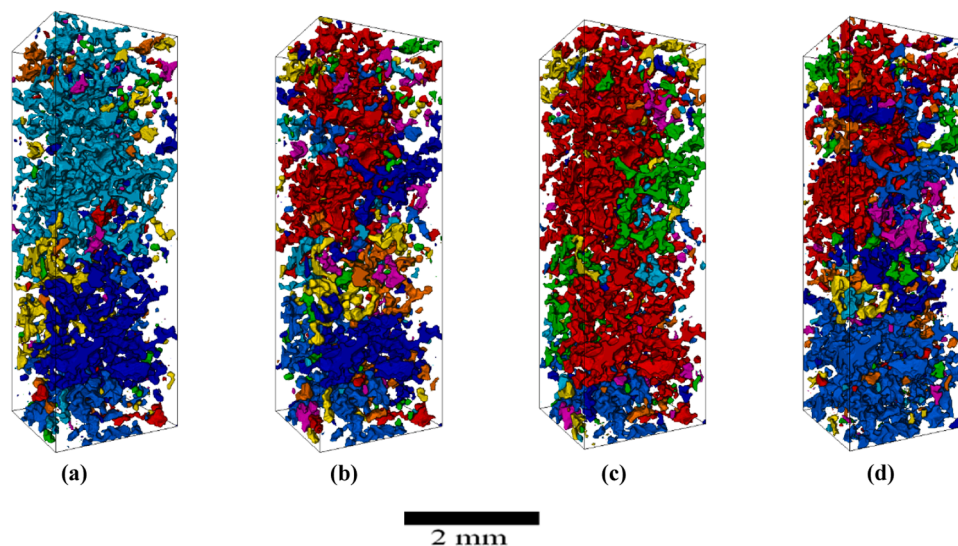| Normalised Euler characteristic	
Pressure (MPa)	$1/mm^3$
10	42
8	10
6	9
5	12
5 (30 hours)	9

Fig. 5. 3D visualization of CO_2 in the pore space: a) 10 MPa, b) 8 MPa, c) 6 MPa, d) 5 MPa. Note that the colors are assigned at random and indicate discrete ganglia of the CO_2.

volume of the image. The results are given in Table 2 as the Euler characteristic per unit volume. The numbers confirm that that under pressure depletion conditions, gas phase connectivity increases once the pressure drops from 10 to 8, and to 6 MPa, indicated by a decrease in Euler number. From 6 to 5 MPa, Euler number increases, and hence poorer connectivity is observed, as the gas is trapped again, which is consistent with the 3D visualizations of CO_2 ganglia in Fig. 5.

3.2. Pore scale ganglia dynamics under no pressure depletion

At the end of the depletion sequence, the system was left to rest for 30 hours to investigate gas-phase redistribution; see Fig. 6. On average across the part of the sample that was imaged, an approximately 10% increase in gas saturation is found: gas may have migrated upwards from the lower part of the sample under gravity. Fig. 7 shows in 3D how after 30 hours the initially dispersed and disconnected gas ganglia are redistributed, creating an enlarged and sizable percolating gas ganglion (shown in blue) that extends the entire length of the sub-volume. The higher gas phase connectivity after 30 hours is confirmed by a fall in Euler characteristic given in Table 2. The increase in saturation implies that exsolution of gas continues over a prolonged period and that equilibrium is not reached instantly. It could also be that on closing the valves, the overall fluid pressure dropped, leading to additional exsolution and gas expansion.

Since the gas is initially trapped at 5 MPa – see Fig. 7 – the redistribution of gas needs to be initiated by both the exsolution of gas and the transport of gas dissolved in the aqueous phase. The merging and reconnection of gas ganglia can be explained by Ostwald ripening, which occurs due to capillary pressure differences among immobile gas ganglia (Li et al., 2021, Blunt, 2022). In this process, the inter-ganglion diffusion of gas dissolved in the aqueous phase is driven by the capillary pressure gradient throughout the sample, causing trapped gas ganglia to either grow or shrink until all the gas ganglia approach the same equilibrium capillary pressure. It is possible that Ostwald ripening in this experiment leads to better connectivity of the gas ganglia, facilitating flow. The time-scales for this phenomenon have been estimated and it is possible to have significant changes in the fluid distribution over distances of a millimeter in the 30 hours of the experiment; equilibrium over larger distances takes a longer, but this local rearrangement is sufficient to reconnect the gas and allow flow (Blunt, 2022, Zhang et al., 2023).

4. Concluding remarks

High-resolution 3D X-ray microtomography was used to characterize pore-scale fluid rearrangement due to the remobilization of residual carbon dioxide during pressure depletion. The pressure range was from 10 to 5 MPa spanning both supercritical and gaseous phases in a water-wet Bentheimer sandstone.
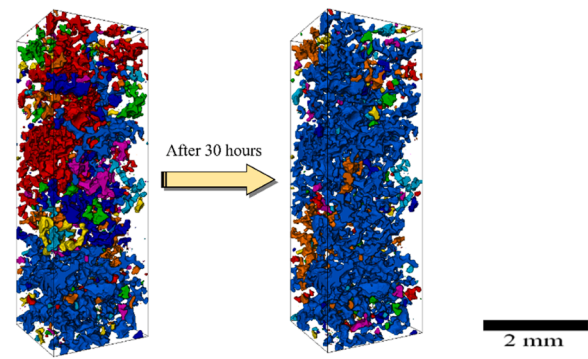

Fig. 7. 3D visualization of CO_2 in the pore space: left) 5 MPa; right) 5 MPa after 30 hours. Note that the colors are assigned at random and indicate discrete ganglia of the CO_2.

After primary drainage followed by subsequent waterflooding the residual gas saturation was large – 0.48 on average. As pressure dropped, gas was produced. This implies that swelling of the gas phase, combined with exsolution, allowed the gas to reconnect through the pore space and flow out of the system. However, when an image was taken, when the pressure was kept constant, in all but one case the gas was disconnected. This implies intermittent production, with the gas phase reconnecting and being produced, followed by the acquisition of a new position of equilibrium where snap-off allows the aqueous phase to strand the gas in larger pores. At one pressure value, the gas was connected across the sample: the average saturation was 0.55, or 0.07 more than the residual value. This may imply that an increase in saturation is required to allow the gas to reconnect and flow. In any event, the intermittent nature of the displacement could explain the low gas relative permeabilities observed on pressure depletion in the literature (Moghadasi et al., 2022, Fishlock et al., 1988, Egermann and Vizika, 2000, Egermann et al., 2010, Xu et al., 2017)

The observations made in this study are consistent with the findings from our field-scale CO_2 injection experiments at Heletz, both in terms of the general behavior and the mobilization saturation. At Heletz, a S_{gmob} value of 0.05, similar to our measured value, and around 90% reduction to gas relative permeability was inferred – under pressure depletion conditions – through extensive history matching and model analysis of the field data (Moghadasi et al., 2022). Furthermore, the observations made in this work closely match the results of pore-network modeling, where the depletion experiment was simulated on extracted networks of Bentheimer and Heletz sandstones which predicted remobilization saturations of 0.064 and 0.061 respectively (Moghadasi et al., 2023). Such studies consistntly applied across field- to pore-scale, significantly improve our understanding of residual gas remobilization and critical saturation in the context of CCS, and in turn enables us to perform more
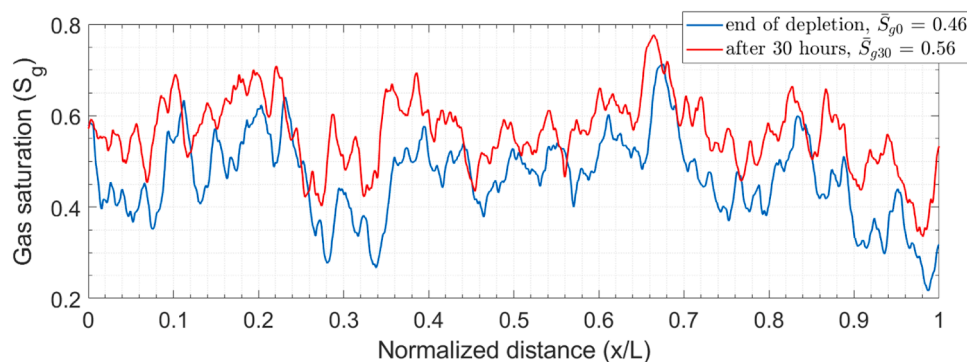

Fig. 6. CO_2 saturation profile at 5 MPa at the end of depletion process (shown in blue) and after 30 hours (shown in red). Average gas saturation for each case is given as $\overline{S}_{g0}$ and $\overline{S}_{g30}$, respectively (x: distance, L: length of the image).

accurate characterization of *in situ* phenomena affecting the security of residual trapping in both the short- and long-term.

At the end of the experiment the system was left for 30 hours and then imaged again. The gas reconnected with an increase in saturation of approximately 0.10 on average. This suggests that continued exsolution combined with Ostwald ripening – the transport of gas dissolved in the aqueous phase to equilibriate local capillary pressure – can lead to reconnection of the gas phase. This implies reduced storage security and trapping: the rearrangement of trapped gas by Ostwald ripening could lead to local reconnection of gas ganglia, which may facilitate flow and enhance migration, thus reducing the amount of CO_2 that can be residually trapped.

We suggest that further research should focus on: (i) investigating this phenomenon at a wider range of pressures and temperatures with consideration of the time-scales to reach equilibrium; (ii) studying the effects of various operational variables such as pressure depletion rate as well as the effects of rock and fluid properties; and (iii) determining the averaged properties, including relative permeability and residual saturation, to use in reservoir simulation models to predict and design carbon dioxide storage. Additionally, we suggest that future studies use brine that is pre-equilibrated with CO_2, to study the sole effects of Ostwald ripening under no pressure depletion. In terms of modeling, future research can validate the existing pore-network simulator (Moghadasi et al., 2023) on a pore-by-pore basis using micro-CT images, and further modify/develop the code to consider Ostwald ripening on its own.

CRediT authorship contribution statement

Ramin Moghadasi: Conceptualization, Formal analysis, Methodology, Writing – original draft. **Sepideh Goodarzi:** Methodology, Software. **Yihuai Zhang:** Methodology, Writing – review & editing. **Branko Bijeljic:** Supervision, Writing – review & editing. **Martin J. Blunt:** Supervision, Writing – review & editing. **Auli Niemi:** Supervision, Writing – review & editing.

Declaration of Competing Interest

The authors declare that they have no known competing financial interests or personal relationships that could have appeared to influence the work reported in this paper.

Data availability

Data (micr-CT images) are publicly available via https://zenodo.org/record/8139724.

Acknowledgements

References

Alcalde, J., et al., 2018. Estimating geological CO2 storage security to deliver on climate mitigation. Nat. Commun. 9, 1–13.

Alhosani, A., et al., 2021. Pore-scale characterization of carbon dioxide storage at immiscible and near-miscible conditions in altered-wettability reservoir rocks. Int. J. Greenh. Gas Control 105, 103232.

Alhosani, A., Selem, A.M., Lin, Q., Bijeljic, B., Blunt, M.J., 2021. Disconnected Gas Transport in Steady-State Three-Phase Flow. Water Resour. Res 57 e2021WR031147.

Ali, M., et al., 2022. Recent advances in carbon dioxide geological storage, experimental procedures, influencing parameters, and future outlook. Earth-Science Rev 225, 103895.

Andrew, M., Bijeljic, B., Blunt, M.J., 2014. Pore-scale imaging of trapped supercritical carbon dioxide in sandstones and carbonates. Int. J. Greenh. Gas Control 22, 1–14.

Berg, S., et al., 2020. Determination of Critical Gas Saturation by Micro-CT. Petrophysics 61, 133–150.

Birkholzer, J.T., Cihan, A., Zhou, Q., 2012. Impact-driven pressure management via targeted brine extraction—Conceptual studies of CO2 storage in saline formations. Int. J. Greenh. Gas Control 7, 168–180.

Blunt, M.J., et al., 2013. Pore-scale imaging and modelling. Adv. Water Resour. 51, 197–216.

Blunt, M.J., Lin, Q., Akai, T., Bijeljic, B., 2019. A thermodynamically consistent characterization of wettability in porous media using high-resolution imaging. J. Colloid Interface Sci. 552, 59–65.

Blunt, M.J., 2022. Ostwald ripening and gravitational equilibrium: Implications for long-term subsurface gas storage. Phys. Rev. E 106, 45103.

Bui, M., et al., 2018. Carbon capture and storage (CCS): the way forward. Energy Environ. Sci. 11, 1062–1176.

Buscheck, T.A., et al., 2011. Combining brine extraction, desalination, and residual-brine reinjection with CO2 storage in saline formations: Implications for pressure management, capacity, and risk mitigation. Energy Procedia 4, 4283–4290.

Celia, M.A., Nordbotten, J.M., Court, B., Dobossy, M., Bachu, S., 2011. Field-scale application of a semi-analytical model for estimation of CO2 and brine leakage along old wells. Int. J. Greenh. Gas Control 5, 257–269.

Egermann, P., Vizika, O., 2000. Critical gas saturation and relative permeability during depressurization in the far field and the near-wellbore region. In: SPE Annual Technical Conference and Exhibition. Society of Petroleum Engineers.

Egermann, P., Schaaf, T., Bréfort, B., 2010. A Modified Hysteresis Relative Permeability Including a Gas Remobilization Threshold For Better Production Forecasts of Gas Storages. Petrophysics 51, 8.

Fishlock, T.P., Smith, R.A., Soper, B.M., Wood, R.W., 1988. Experimental Studies on the Waterflood Residual Gas Saturation and Its Production by Blowdown. SPE Reserv. Eng. 3, 387–394.

Goodman, A., et al., 2011. US DOE methodology for the development of geologic storage potential for carbon dioxide at the national and regional scale. Int. J. Greenh. Gas Control 5, 952–965.

Herring, A.L., Robins, V., Sheppard, A.P., 2019. Topological persistence for relating microstructure and capillary fluid trapping in sandstones. Water Resour. Res. 55, 555–573.

Iglauer, S., Paluszny, A., Pentland, C.H., Blunt, M.J., 2011. Residual CO2 imaged with X-ray micro-tomography. Geophys. Res. Lett. 38, 1–6.

IPCC. Carbon dioxide capture and storage. Special Report. (2005).

Jiang, P., et al., 2014. Thermal modeling of CO2 in the injection well and reservoir at the Ordos CCS demonstration project, China. Int. J. Greenh. gas Control 23, 135–146.

Joodaki, S., et al., 2020. Model analysis of CO2 residual trapping from single-well push pull test—Heletz, Residual Trapping Experiment II. Int. J. Greenh. Gas Control 101, 103134.

Kortekaas, T.F.M., van Poelgeest, F., 1991. Liberation of solution gas during pressure depletion of virgin and watered-out oil reservoirs. SPE Reserv. Eng. 6, 329–335.

Krevor, S., et al., 2015. Capillary trapping for geologic carbon dioxide storage–From pore scale physics to field scale implications. Int. J. Greenh. Gas Control 40, 221–237.

Lebedev, M., Zhang, Y., Mikhaltsevitch, V., Inglauer, S., Rahman, T., 2017. Residual Trapping of Supercritical CO2: Direct Pore-scale Observation Using a Low Cost Pressure Cell for Micro Computer Tomography. Energy Procedia 114, 4967–4974.

Lebedev, M., et al., 2017. Carbon geosequestration in limestone: Pore-scale dissolution and geomechanical weakening. Int. J. Greenh. Gas Control 66, 106–119.

Li, X., Yortsos, Y.C., 1993. Critical gas saturation: modeling and sensitivity studies. In: SPE Annual Technical Conference and Exhibition. Society of Petroleum Engineers.

Li, X., Yortsos, Y.C., 1995. Visualization and simulation of bubble growth in pore networks. AIChE J 41, 214–222.

Li, Y., Orr, F.M., Benson, S.M., 2021. Long-Term Redistribution of Residual Gas Due to Non-convective Transport in the Aqueous Phase. Transp. Porous Media 1–23.

Ligthelm, D.J., Reijnen, G., Wit, K., Weisenborn, A.J., Scherpenisse, W., 1997. Critical gas saturation during depressurisation and its importance in the Brent field. In: Offshore Europe. Society of Petroleum Engineers.

Lin, Q., Bijeljic, B., Pini, R., Blunt, M.J., Krevor, S., 2018. Imaging and measurement of pore-scale interfacial curvature to determine capillary pressure simultaneously with relative permeability. Water Resour. Res. 54, 7046–7060.

McDougall, S.R., Sorbie, K.S., 1999. Estimation of critical gas saturation during pressure depletion in virgin and waterflooded reservoirs. Pet. Geosci. 5, 229–233.

Megawatsoft. CO2 tables calculator. https://www.carbon-dioxide-properties.com/co2tablesweb.aspx.

Michael, K., et al., 2010. Geological storage of CO2 in saline aquifers—A review of the experience from existing storage operations. Int. J. Greenh. gas Control 4, 659–667.

Moghadasi, R., Basirat, F., Bensabat, J., Doughty, C., Niemi, A., 2022. Role of critical gas saturation in the interpretation of a field scale CO2 injection experiment. Int. J. Greenh. Gas Control 115, 103624.

Moghadasi, R., 2022. Residual and critical saturation in geological storage of CO2 : results from field studies, pore-network modelling and laboratory experiments. Digital Comprehensive Summaries of Uppsala Dissertations from the Faculty of Science and Technology NV - 2216. Acta Universitatis Upsaliensis.

Moghadasi, R., et al., 2023. Pore-scale determination of residual gas remobilization and critical saturation in geological CO2 storage: a pore-network modeling approach. Water Resour. Res. 59, e2022WR033686 https://doi.org/10.1029/2022WR033686.

Niemi, A., Bear, J., Bensabat, J., 2017. Geological storage of CO2 in deep saline formations, 29. Springer.

Niemi, A., et al., 2020. Characterizing CO2 residual trapping in-situ by means of single-well push-pull experiments at Heletz, Israel, pilot injection site–experimental procedures and results of the experiments. Int. J. Greenh. Gas Control 101, 103129.

Peksa, A.E., Wolf, K.-H.A.A., Zitha, P.L.J., 2015. Bentheimer sandstone revisited for experimental purposes. Mar. Pet. Geol. 67, 701–719.

Qi, R., LaForce, T.C., Blunt, M.J., 2009. Design of carbon dioxide storage in aquifers. Int. J. Greenh. Gas Control 3, 195–205.

Raeini, A.Q., Giudici, L.M., Blunt, M.J., Bijeljic, B., 2022. Generalized network modelling of two-phase flow in a water-wet and mixed-wet reservoir sandstone: Uncertainty and validation with experimental data. Adv. Water Resour. 164, 104194.

Rasmusson, K., et al., 2018. Residual trapping of carbon dioxide during geological storage—Insight gained through a pore-network modeling approach. Int. J. Greenh. Gas Control 74, 62–78.

Shaffer, G., 2010. Long-term effectiveness and consequences of carbon dioxide sequestration. Nat. Geosci. 3, 464–467.

Shi, J.-Q., et al., 2013. Snøhvit CO2 storage project: Assessment of CO2 injection performance through history matching of the injection well pressure over a 32-months period. Energy Procedia 37, 3267–3274.

Singh, K., et al., 2017. Dynamics of snap-off and pore-filling events during two-phase fluid flow in permeable media. Sci. Rep. 7, 1–13.

ToolBox, E. Carbon Dioxide - Thermophysical Properties. https://www.engineeringtoolbox.com/CO2-carbon-dioxide-properties-d_2017.html.

Wim Dubelaar, C., Nijland, T.G., 2015. The Bentheim Sandstone: geology, petrophysics, varieties and its use as dimension stone. In: Engineering Geology for Society and Territory-Volume, 8. Springer, pp. 557–563.

Xu, R., Li, R., Huang, F., Jiang, P., 2017. Pore-scale visualization on a depressurization-induced CO2 exsolution. Sci. Bull. 62, 795–803.

Yu, H., et al., 2019. CO2-Saturated Brine Injection Into Unconsolidated Sandstone: Implications for Carbon Geosequestration. J. Geophys. Res. Solid Earth 124, 10823–10838.

Zhang, D., Song, J., 2014. Mechanisms for geological carbon sequestration. Procedia IUTAM 10, 319–327.

Zhang, Z., Kruschwitz, S., Weller, A., Halisch, M., 2018. Enhanced pore space analysis by use of μ-CT, MIP, NMR, and SIP. Solid Earth 9, 1225–1238.

Zhang, Y., et al., 2023. Pore-Scale Observations of Hydrogen Trapping and Migration in Porous Rock: Demonstrating the Effect of Ostwald Ripening. Geophys. Res. Lett. 50 e2022GL102383.